NISTIR 89-4111

TOUGHENING MECHANISMS IN CERAMIC COMPOSITES

SEMI-ANNUAL PROGRESS REPORT FOR THE PERIOD ENDING MARCH 31, 1989

E. R. Fuller, Jr.
E. P. Butler
R. F. Krause, Jr.
M. D. Vaudin

U.S. DEPARTMENT OF COMMERCE
National Institute of Standards
and Technology
Ceramics Division
Gaithersburg, MD 20899

U.S. DEPARTMENT OF COMMERCE
Robert A. Mosbacher, Secretary
NATIONAL INSTITUTE OF STANDARDS
AND TECHNOLOGY
Raymond G. Kammer, Acting Director

NIST

NISTIR 89-4111

TOUGHENING MECHANISMS IN CERAMIC COMPOSITES

SEMI-ANNUAL PROGRESS REPORT FOR THE PERIOD ENDING MARCH 31, 1989

E. R. Fuller, Jr.
E. P. Butler
R. F. Krause, Jr.
M. D. Vaudin

U.S. DEPARTMENT OF COMMERCE
National Institute of Standards
and Technology
Ceramics Division
Gaithersburg, MD 20899

Prepared for
U.S. Department of Energy
Fossil Energy
Advanced Research & Technology
Development
Fossil Energy Materials Program
Oak Ridge National laboratory
Oak Ridge, TN

July 1989

Interagency Agreement
DE-A105-800R206179

U.S. DEPARTMENT OF COMMERCE
Robert A. Mosbacher, Secretary
NATIONAL INSTITUTE OF STANDARDS
AND TECHNOLOGY
Raymond G. Kammer, Acting Director

TOUGHENING MECHANISMS IN CERAMIC COMPOSITES

Semi-Annual Progress Report for the Period Ending March 31, 1989 *

Prepared for U.S. Department of Energy, Fossil Energy
Advanced Research & Technology Development
Fossil Energy Materials Program
Oak Ridge National Laboratory
Oak Ridge, TN

Interagency Agreement DE-AI05-80OR20679

E. R. Fuller, Jr., E. P. Butler,
R. F. Krause, Jr., and M. D. Vaudin

National Institute of Standards and Technology
Institute for Materials Science and Engineering
Ceramics Division
Gaithersburg, MD 20899

INTRODUCTION

The achievement of higher efficiency heat engines and heat recovery systems requires the availability of high-temperature, high-performance structural materials. Structural ceramics and, more recently, ceramic matrix composites have received particular attention for these applications due to their high strength and excellent resistance to corrosion, erosion and thermal shock. Even with these positive attributes, improved reliability and extended lifetime under service conditions are necessary for structural ceramics and ceramic composites to gain wide industrial acceptance. This reliability is only achieved with improved knowledge of in-service damage modes and failure mechanisms, and the processing knowledge to improve this performance by microstructural modifications. The inherent problems are mechanical and chemical in nature and are enhanced by the high temperatures, reactive environments, and extreme thermal gradients and thermal cycling, to which these materials are subjected.

With an objective of improved performance for heat engine/heat recovery applications, the NIST program addresses these problems through a determination and characterization of major toughening mechanisms in ceramic composites, examining both model crack-fiber systems and "real" composites. A key aspect of the program is a determination of the critical processing factors which influence microstructure and interfacial behavior in these materials, and which thereby influence these toughening mechanisms. The activities of the program are grouped under two major work areas, each designed to develop key data, associated test methods and companion predictive models. The status of these two work areas are detailed below.

---

* Also in ORNL/FMP-89/1, Fossil Energy Materials Program, R. R. Judkins, Manager, Oak Ridge National Laboratory, Oak Ridge, TN, 1989.

DISCUSSION OF CURRENT ACTIVITIES

NIST-1.1. Crack-Fiber Interactions.

Interface Properties of a Model Composite System with Metallic Interlayers

Summary. The toughening effect that fibers and whiskers engender to brittle ceramics arises from several phenomena, including crack deflection, reinforcement/matrix debonding, crack bridging, and frictional pullout. These characteristics are dependent upon the fiber/whisker radius and length, the physical properties of the reinforcement and the matrix, the interfacial chemistry, and the stress state at the interface. In current activities we have concentrated on the interface between the reinforcement and the matrix. Residual stresses at this interface arise primarily from the thermal expansion mismatch between the reinforcement and the matrix, but are influenced by the chemistry of the interfacial bond and the rheological properties of the matrix during processing. This second factor is particularly important for glass matrices. Both factors are processing sensitive so that the residual stresses at the interface at room temperature are thermal history dependent.

In the present study we examine the influence of a ductile interfacial layer on the toughening effect that a single SiC fiber engenders to a brittle glass matrix. The interface mechanics of the system are addressed both as a fiber debond/pullout problem and as a crack/fiber interaction problem.

Background. Previous work in this area[1,2,3], using the model composite system of SiC monofilaments [ACVO SCS-6 SiC] as a reinforcement in a borosilicate glass matrix [Pyrex glass, #7740], has shown that enhanced crack resistance can be built into the glass. The toughening increment has been shown to be as much as 22% for reinforcement by a single fiber. The work presented here builds upon this experience and examines the influence of metallic interlayers on this toughening increment.

Sample Fabrication. Test specimens were fabricated by diffusion bonding of the fibers between borosilicate glass plates as detailed in a previous report[1]. Specimens were prepared with the fiber surface in the as-received condition as well as with a thin metallic nickel coating. The nickel was electrodeposited on the fiber surface to various thicknesses between 1 μm and 22 μm.

The processing conditions for each specimen is detailed in Table 1; nominally each specimen was fabricated under similar conditions. The maximum processing temperature for each specimen was 706°C, after which the specimen was cooled to room temperature at nominally the same rate. Accordingly, the rheological response of the glass matrix should be the same for these studies, and the only variable affecting the interfacial properties should be the presence of the metallic interfacial layer and its thickness.

Table 1. Fabrication Conditions for Mechanical Test Samples.

FIBER COATING	TIME AT 660°C	TIME AT 706°C
none	3hrs:25min	2hrs:20min
1 μm Nickel	3:40	1:45
9 μm Nickel	3:35	1:55
22 μm Nickel	4:00	1:55

Fiber Pullout Test. Assessment of the influence of the metallic interfacial layer on the micromechanics of the matrix/nickel/fiber interfaces was achieved using the single fiber pullout test. The test geometry and equipment used were described in the previous report[1].

Figure 1 shows a typical fiber pullout test. The debond shear strength, S_d, of the fiber/matrix interface is given by

$$S_d = P_d/2rl \tag{1}$$

where P_d is the debond load, r is the fiber radius, and l is the embedded length of fiber in the matrix. The average frictional shear resistance, τ, is given by

$$\tau = P_f/2rl \tag{2}$$

where P_f is the load as the fiber begins to slide. Eqs. (1) and (2) are an approximation to the actual behavior, but are sufficient for the present.

As seen in Figure 2, the debond shear strength and the frictional shear resistance are sensitive to the thickness of the nickel coating. The uncoated fiber has the highest debond strength and frictional resistance. As the thickness of the nickel coating is increased these two stresses continue to decrease with the 22 μm coated fiber having the lowest values.

Examination of the specimen after the pullout test revealed that the fibers pulled away from the nickel coating leaving it still bonded to the glass matrix. Thus, it appears that the SiC fiber/nickel interface is weaker than the nickel/glass interface and has a lower sliding friction.

Fracture Resistance Behavior. The double-cleavage, drilled-compression (DCDC) test geometry was used to assess the fracture resistance behavior of the nickel coated fiber in comparison to the uncoated fiber in the glass matrix. The change in applied stress intensity factor, K_I, as a crack propagated perpendicular to the reinforcing fiber was monitored as a function of crack extension for both coated and uncoated specimens. Two tests were conducted for each composite. The results are shown in Fig. 3.

All fibers, regardless of surface preparation, gave an enhanced toughness to the glass composite compared to that of the unreinforced glass. No fibers broke in the path of the advancing crack, but were all debonded and frictionally pulled out. Scatter in the results makes it difficult to assess the effectiveness of the nickel coating from the applied stress versus crack length curves. The toughening effect of the fiber can be quantified as an incremental toughening parameter, K_{Imax}/K_{IC}, where K_{Imax} is the maximum applied stress intensity factor and K_{IC} is the fracture toughness of the unreinforced glass (0.77 $MPa\cdot\sqrt{m}$ in this case). This factor is plotted in Figure 4 versus the fiber coating thickness.

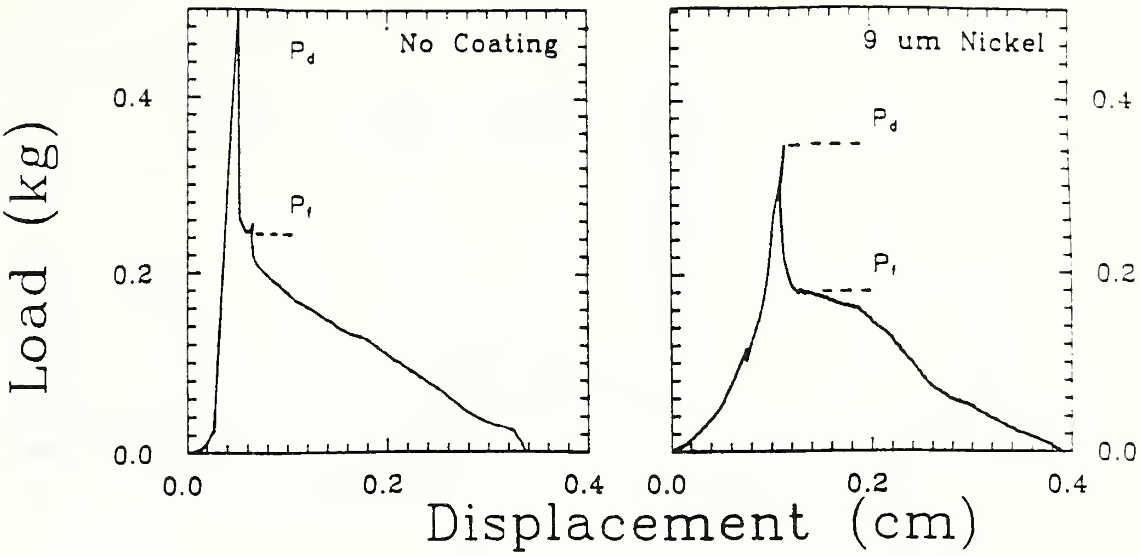

Figure 1. Load-displacement curves for single fiber pull-out tests: (a) Uncoated SiC fiber in glass matrix and (b) Nickel-coated SiC fiber in glass matrix.

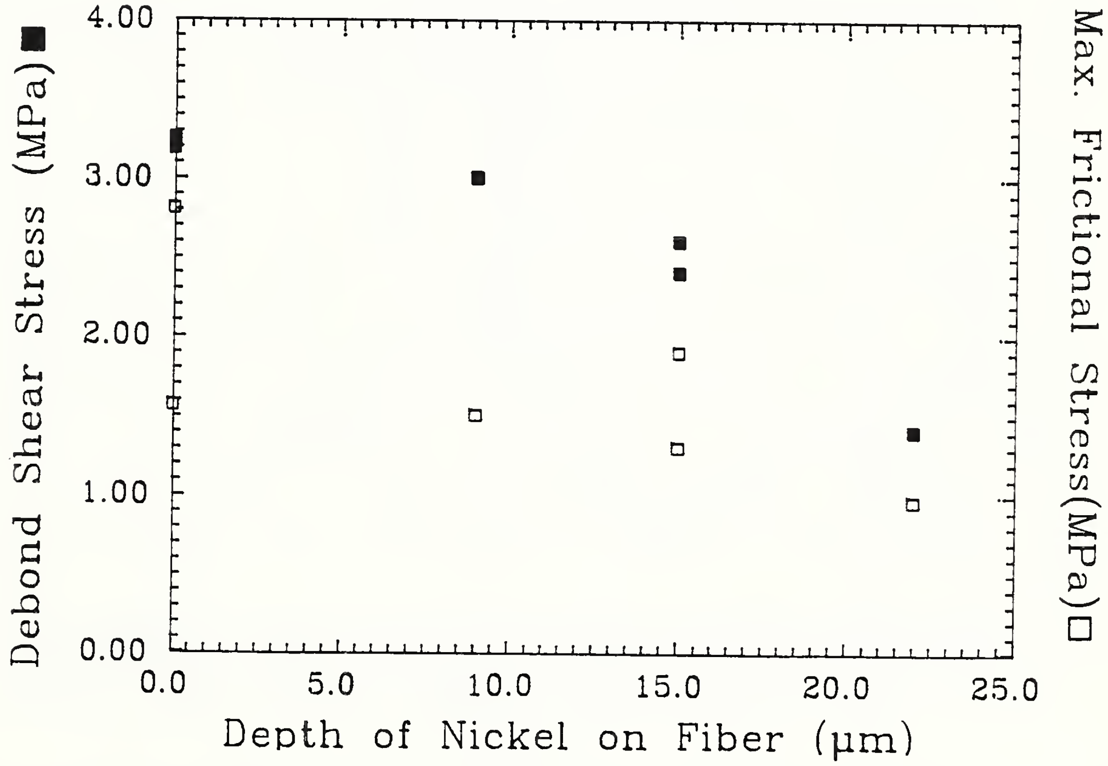

Figure 2. Debond shear stress (filled squares) and frictional pull-out stress (open squares) as a function of fiber coating thickness.

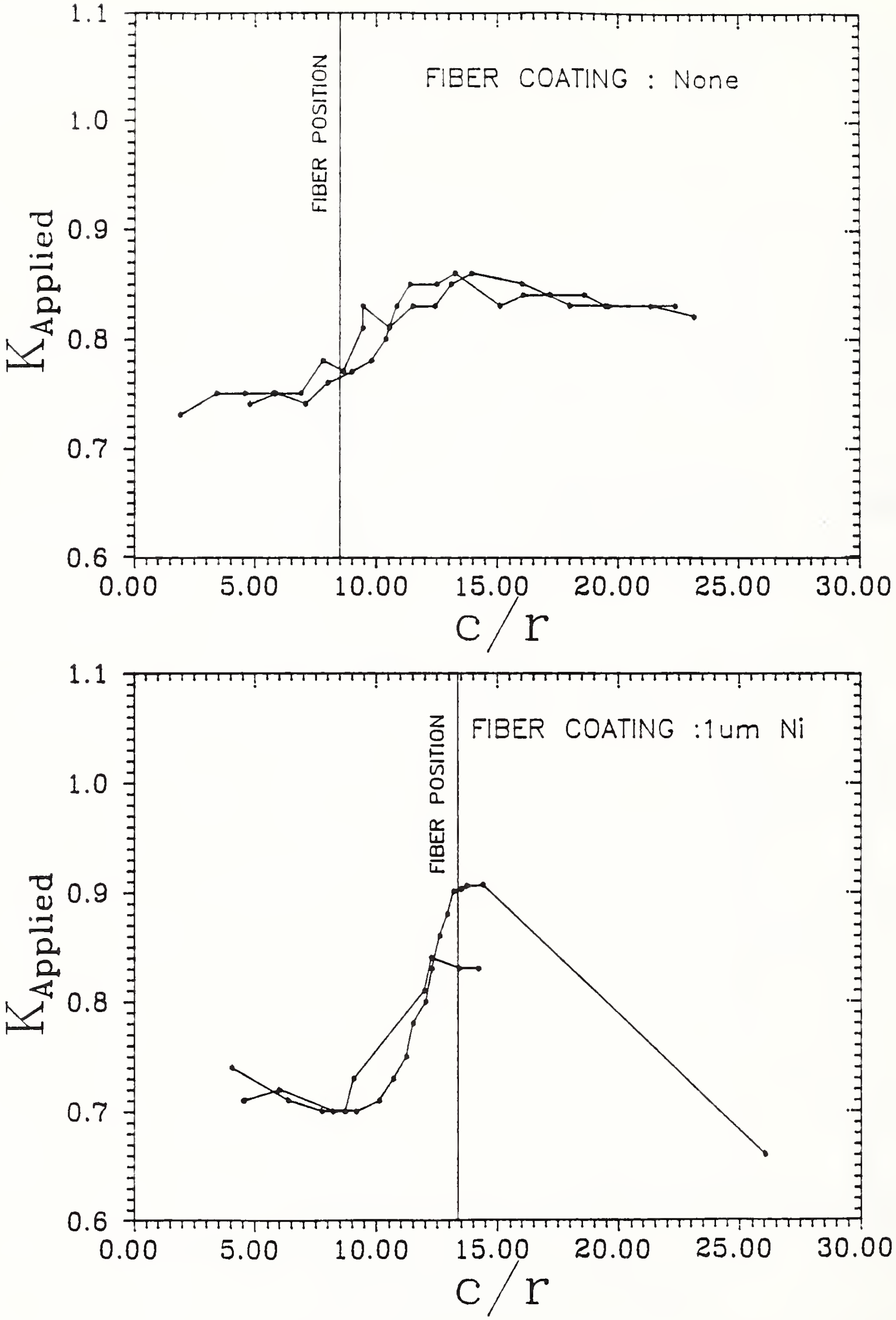

Figures 3a and 3b. Applied stress intensity factor as a function of crack size for the DCDC-fracture mechanics specimen.

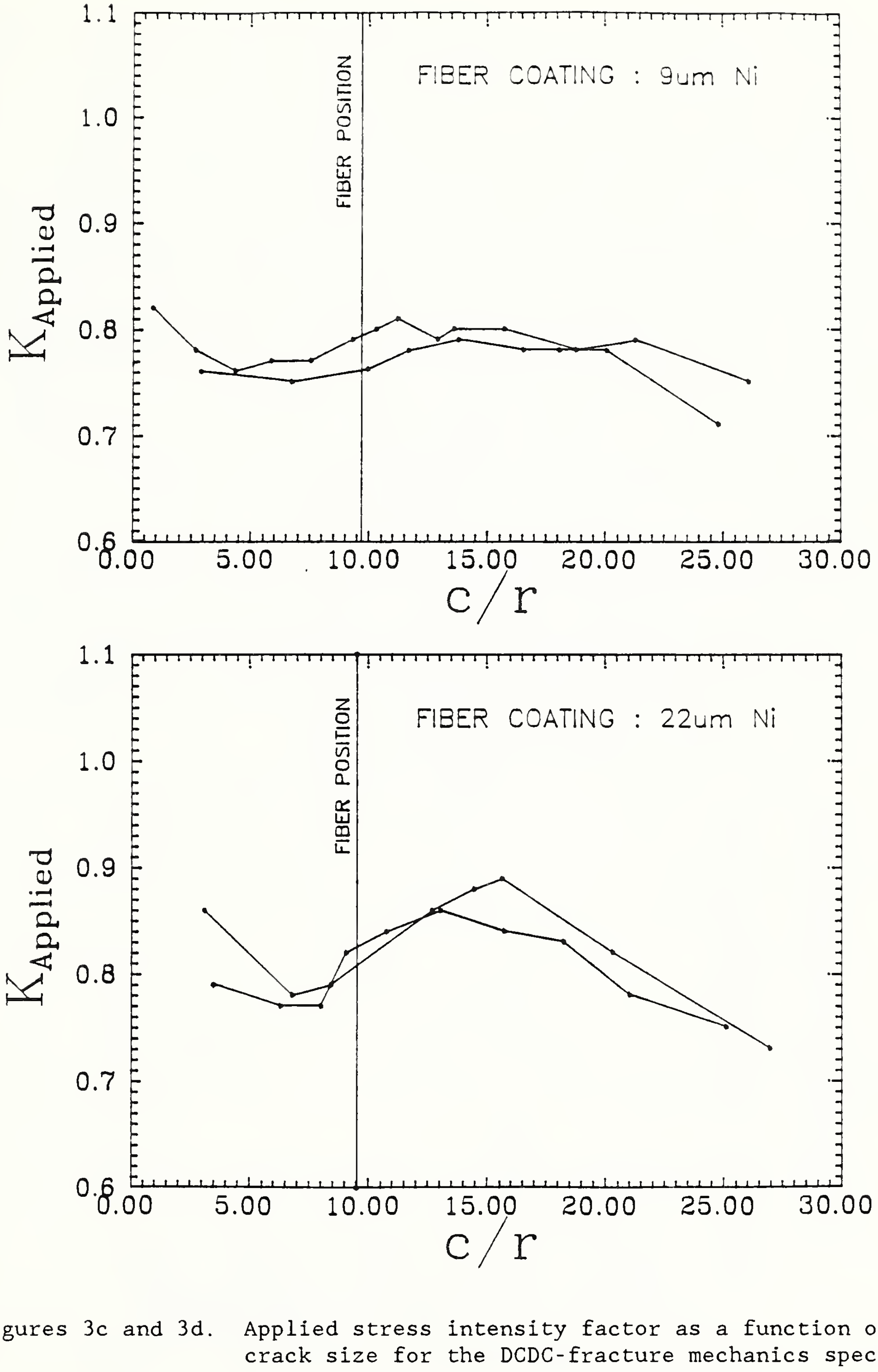

Figures 3c and 3d. Applied stress intensity factor as a function of crack size for the DCDC-fracture mechanics specimen.

We might expect the same trend in toughening behavior with coating thickness as the debond strength and frictional shear resistance, that is a decreasing toughness increment with increasing coating thickness. This has not unequivocally been observed. The majority of the specimens with coated fibers did indeed have a lower toughness, but two specimens (one at 1 μm and one at 22 μm) had greater toughness than the uncoated fiber reinforced specimens. It is well to keep in mind that the pullout tests primarily measured the fiber/nickel interface, which was weaker than the fiber/glass interface. However, when a crack interacts with the reinforcement it first encounters the glass/nickel interface. If debonding occurs on this interface, the fiber with its nickel coating intact will frictionally pullout and the crack can only later interact with the nickel/SiC interface. Thus, low interfacial strength of the nickel/SiC interface does not necessarily produce a low toughening increment.

In summary, metallic coating on reinforcing fibers offer interesting possibilities for enhanced toughening of ceramic composites. However, evidence to date is not conclusive. Further work will concentrate on improving the processing conditions so that a variety of glass/metal and metal/fiber interface conditions can be examined.

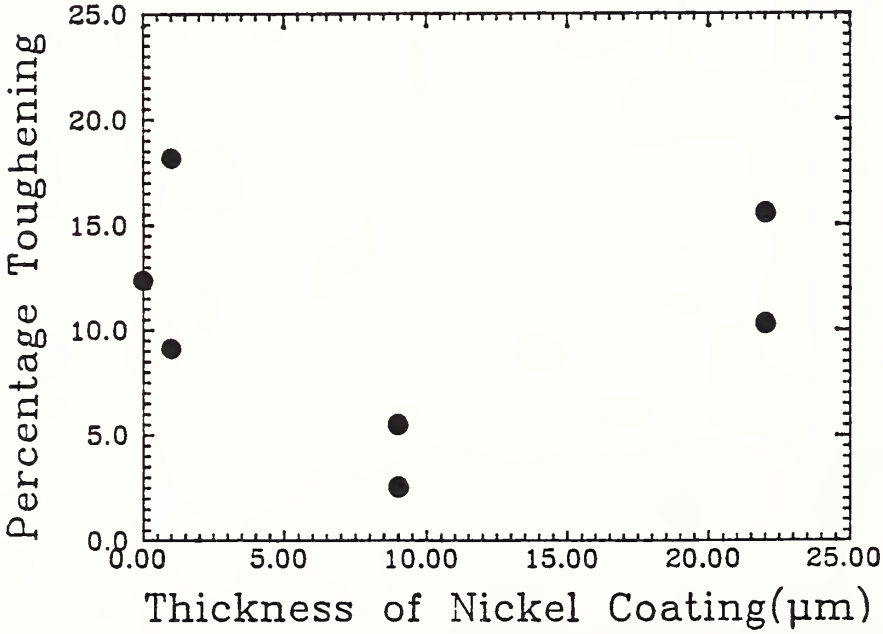

Figure 4. Toughening increment as a function of fiber coating.

NIST-1.2. Real Ceramic Composite Systems.

A. Creep Behavior of a SiC Whisker-Reinforced Al_2O_3 Composite

Summary. Time functions of creep strain and creep times to failure were measured for a 25 wt% SiC whisker-reinforced Al_2O_3 composite with 4.9% porosity. Beam specimens were used in four-point flexure with variously fixed bending moments and fixed temperatures between 1100 and 1300°C. The overall range of initial stresses on the outer fiber due to the bending moments varied from 55 to 306 MPa, but the range at each temperature was narrower. Creep strains were determined from load-point displacement measurements. The results of 34 experiments were outlined earlier[1].

In the current reporting period the results were analyzed to evaluate secondary creep-strain rate as a function of the initial stress on the outer fiber, of temperature, and of time to failure. Typically, the observed time function of creep strain for each individual beam specimen exhibited two regions of behavior: (1) a primary creep mode where the rate decreased with time and (2) a secondary creep mode where the rate was invariant with time. A customary model for the time function of creep strain was adopted to represent both regions of behavior for all the creep tests. Application of this model yields secondary strain rates that appear to have endured generally over more than half the duration of those creep tests which ended with specimen failure. These rates vary from $6x10^{-8}$ to $3x10^{-3}$ h^{-1}, assuming both linear creep with applied stress and no displacement of the neutral axis of flexure from the geometric center.

At fixed temperatures the relationship of secondary strain rate versus initial stress indicates two regions of behavior which could be separated by a threshold stress. Norton's power-law function of stress[4] represents the secondary strain rate at stresses above the threshold, but the secondary strain rate at stresses below the threshold are much lower than what Norton's function predicts and were often barely detectable.

A least-squares fit of Norton's function of stress and of Arrhenius' function of temperature was applied to those secondary creep-strain rates at stresses above the threshold stress at each temperature. The results give a creep index of 5.4 ± 0.4 and an activation energy of

904 ± 40 kJ/mol, where the uncertainties are standard deviations from 21 tests. Creep strains at failure were observed in 22 tests to vary roughly from 0.2% at 1100°C to 2% at 1300°C. The secondary strain rates in these tests are represented by Monkman-Grant's function of time to failure, varying from 0.5 to 1000 h.

Applied Stress and Creep Strain. The applied stress, σ, in four-point flexure and the corresponding creep strain, ϵ, were calculated by the method of Hollenberg, Terwilliger, and Gordon[5]. Their approach assumes the constitutive law of a material, namely, that the strain (and strain rate) can be separated into individual functions of stress and time, t, as

$$\epsilon(t,\sigma) = \sigma^n J(t) \tag{3}$$

where n is the creep index and J(t) is creep compliance. Using the constitutive law, they developed expressions which relate σ and ϵ to the creep index, the applied load, F, and the load-point displacement, y. Their expressions are briefly described below.

When the neutral axis of flexure is assumed to be at the center of the beam, the stress on the outer fiber of the beam is given by

$$\sigma/\sigma_1 = (2n+1)/3n \tag{4}$$

where σ_1 is the initial linear elastic stress on the outer fiber,

$$\sigma_1 = 3F(\ell_2 - \ell_1)/2bh^2 \tag{5}$$

In the present work the major and minor loading spans were $\ell_2 = 40$ mm and $\ell_1 = 10$ mm, respectively, and the beam dimensions were $b = 4$ mm and $h = 3$ mm.

The corresponding creep strain of the outer fiber is given by

$$\epsilon/\epsilon_1 = (n+2)(\ell_2+2\ell_1)/3[\ell_2+\ell_1(n+1)] \tag{6}$$

where ϵ_1 is analogous to linear elastic strain,

$$\epsilon_1 = 6hy/(\ell_2^2+\ell_1\ell_2-2\ell_1^2) \tag{7}$$

Since the creep index, n, has yet to be evaluated, only the linear-creep values of stress and strain, σ_1 and ϵ_1, can be evaluated from Eqs. (5) and (7), respectively, at this stage of the analysis.

Time Function of Creep Strain. A customary creep model[6] was adopted to represent creep strain as a function of time. This model consists of an elastic element in parallel with a viscous element, and this compound is in series with another viscous element. The model gives the time function of creep strain as

$$\epsilon = \epsilon_{so}[1 - \exp(-t/\tau)] + \dot{\epsilon}_s t \tag{8}$$

where $\dot{\epsilon}_s$ is the secondary creep-strain rate, ϵ_{so} is the y-intercept of creep strain of the secondary mode, $\tau = \epsilon_{so}/(\dot{\epsilon}_o-\dot{\epsilon}_s)$, and $\dot{\epsilon}_o$ is the initial creep-strain rate. The identity of these parameters is consistent with the derivative of Eq. (8), namely,

$$\dot{\epsilon} = (\epsilon_{so}/\tau)\exp(-t/\tau) + \dot{\epsilon}_s \tag{9}$$

Figure 5 shows a typical time function of creep strain for a flexure specimen with a fixed bending moment at a fixed temperature. The solid curve shows creep strain, ϵ_1, which was calculated from Eq.(7), and reflects load-point displacement which was measured as a function of time. Preliminary values of the coefficients, $\dot{\epsilon}_s$, ϵ_{so} and τ, were estimated by a least-squares fit of Eq. (8) in which ϵ_1 was substituted for ϵ. The dashed curves in Figure 5 show the corresponding predicted values of strain and strain rate from Eqs. (8) and (9), respectively. In the same manner secondary strain rates, $\dot{\epsilon}_s$, were estimated for all of the creep tests. While the predicted strain curves generally deviated from the observed strain curves in a systematic pattern as indicated in Figure 5, the deviations were generally within the 10^{-4} sensitivity of the strain measurements.

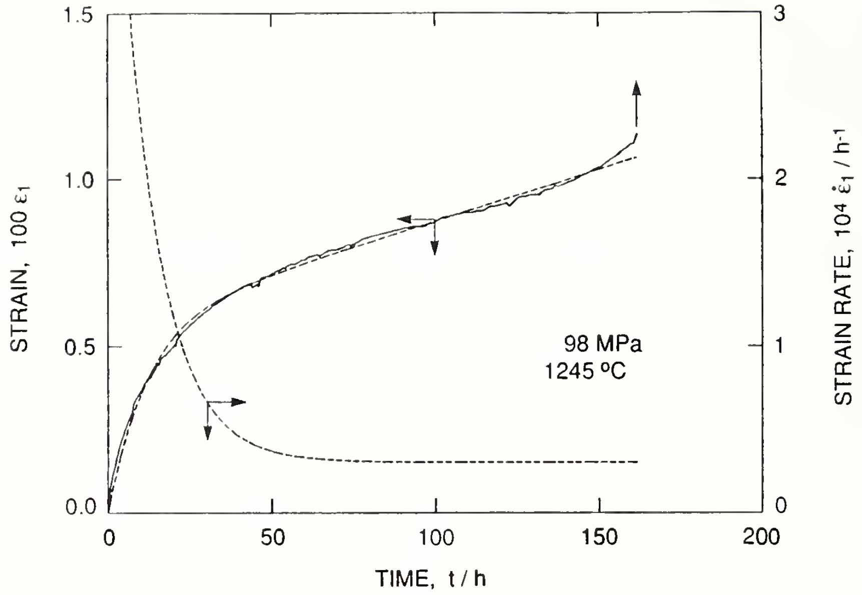

Figure 5. Typical creep strain as a function of time for a flexure specimen with a fixed bending moment at a fixed temperature. The solid curve reflects load-point displacement measurements. The dashed curves show predictions of strain and strain rate from a least-square fit.

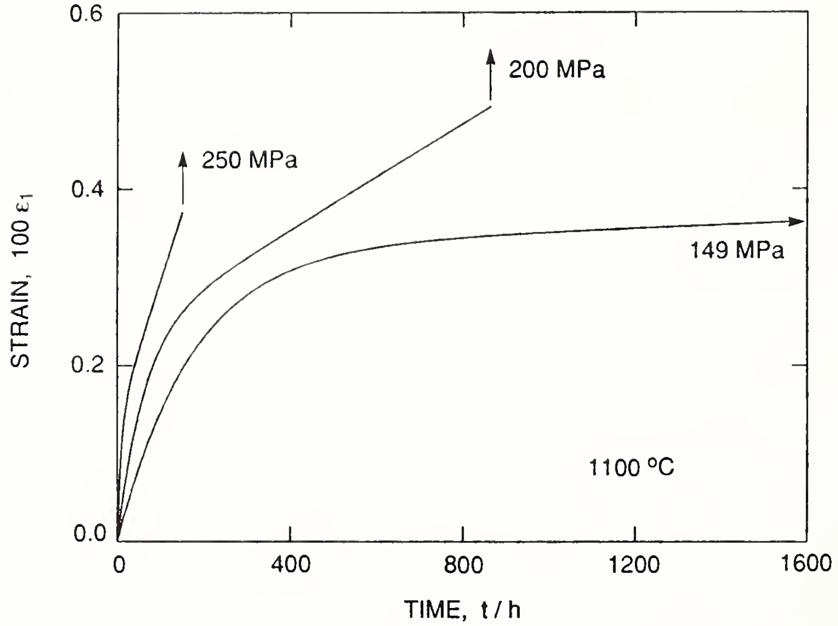

Figure 6. Selected curves of creep strain as a function of time. These curves are predictions from least-squares fits. Notice that the test of longest duration approaches a barely detectable strain rate.

Figure 6 shows time functions of creep strain for creep tests at selected bending moments and the same temperature. Notice that primary creep persisted for a prolonged period, but eventually secondary creep appears to be have been attained and to have endured approximately 2/3 the duration of the tests shown. The ratio of initial strain rate to secondary strain rate, $\dot{\epsilon}_o/\dot{\epsilon}_s$, varies from 1700 to 800 to 90 for these tests at 149 MPa, 200 MPa, and 250 MPa, respectively. It is important to identify the secondary creep mode in order to evaluate a proper value of strain rate which is invariant with time; otherwise a strain rate taken from the primary mode would be seriously overestimated. This problem is especially likely to arise when creep tests at low bending moments are prematurely discontinued. Several hundred hours may be required to attain the secondary mode, and thousands of hours required before the test ends in failure.

The creep index, n, can be evaluated at a given temperature as the following slope,

$$n = d\log(\dot{\epsilon}_s)/d\log(\sigma) \tag{10}$$

Corresponding valves of σ_1 and ϵ_1 from Eqs. (5) and (7), respectively, can be appropriately substituted in Eq. (10) because the constant factors on the right-hand side of Eqs. (4) and (6) merely shift the logarithmic scales. Figure 7 shows these estimates of secondary creep-strain rates as a function of applied stress for all the various creep tests conducted to date. The solid circles at each temperature in Figure 7 seem to follow straight-line functions whose slopes can be described by the same creep index, which will be evaluated below; but the open circles are generally much lower than what these solid lines would predict, indicating a threshold of stress at the respective temperatures. The creep curve at the stress of 149 MPa in Figure 6, for example, gives a secondary strain rate that is plotted as an open circle in Figure 7. Although this curve shows a considerable amount of primary creep strain, its secondary creep-strain rate is so small as to be barely detectable; and this creep test has endured for an exceedingly long time.

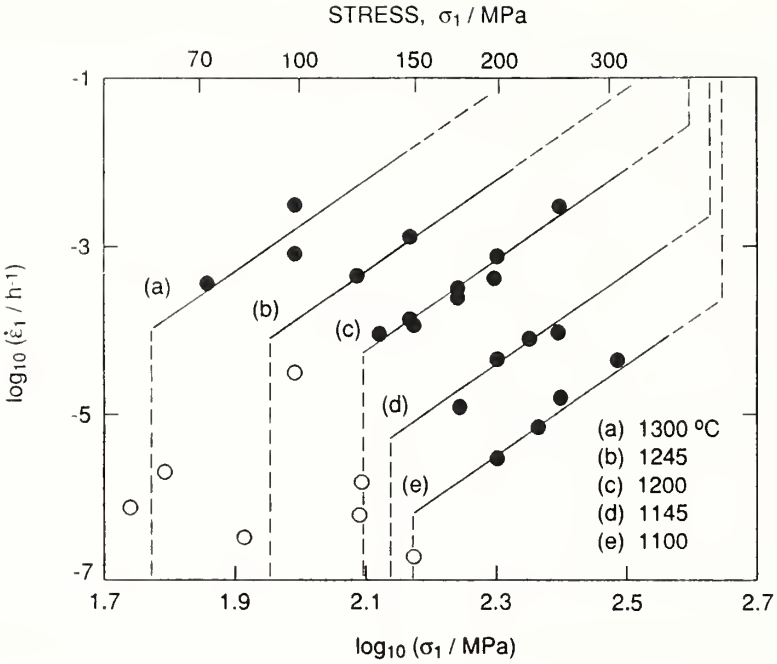

Figure 7. Secondary creep-strain rate as Norton's function of initial stress at selected temperatures. The open circles near the leftward, vertical-dashed lines show exceedingly low strain rates, indicating a threshold of stress. The rightward vertical-dashed lines indicate strengths by rapid loading.

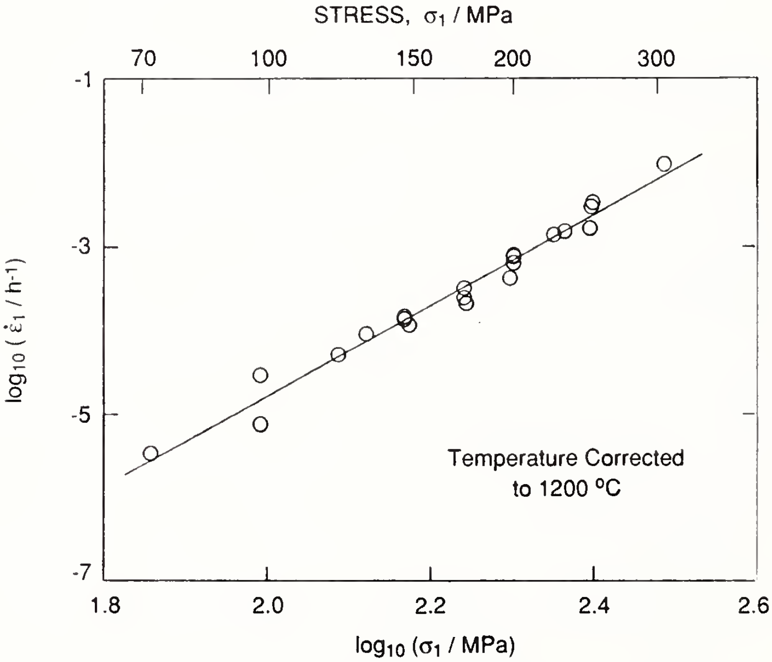

Figure 8. Secondary creep-strain rate as Norton's function of initial stress. Those points which were observed at temperatures other than 1200°C were temperature-corrected to 1200°C. The solid line is a least-squares fit.

Stress and Temperature Functions. The secondary creep-strain rate can usually be described by the product of Norton's power-law function of applied stress and Arrhenius' function of temperature,

$$\dot{\epsilon}_s = A \cdot \sigma^n \cdot \exp(-Q/RT) \tag{11}$$

where A is a constant, Q is the creep activation energy, T is the absolute temperature, and $R = 8.3143\ J \cdot K^{-1} mol^{-1}$. The logarithm of Eq. (11) was fitted by a method of least-squares to represent those secondary creep-strain rates which are the solid circles in Figure 7. The results give $\log_{10}(A) = 16.4 \pm 0.8$ for $\dot{\epsilon}_s$ in h^{-1} and σ in MPa, $n = 5.4 \pm 0.4$, and $Q = 904 \pm 40$ kJ/mol, where the uncertainties are standard deviations for 21 experiments. Figures 8 and 9 show the stress and temperature functions, respectively, for the secondary creep-strain rates. The σ_1 and ϵ_1 shown in these plots can be corrected by $\sigma/\sigma_1 = 0.73$ and $\epsilon/\epsilon_1 = 1.42$, using $n = 5.4$ in Eqs. (4) and (6), respectively. The points in Figures 8 and 9 are observed values which were temperature-corrected and stress-corrected, respectively, using the least-squares fitted values of the coefficients in Eq. (11).

Creep Time to Failure. The empirical expression proposed by Monkman and Grant[7] has had a significant influence on the development of creep fracture models. The general form of their expression is given as

$$\dot{\epsilon}_s{}^{\beta} \cdot t_f = C \tag{12}$$

where t_f is the duration of the creep test to specimen failure, and β and C are constants. The logarithm of Eq. (12) was fitted by a least-squares method to evaluate the coefficients, $\beta = 0.78 \pm 0.07$ and $C = 0.031 \pm 0.022$ in hour time units, where the uncertainties are standard deviations for 22 measurements. Figure 10 shows the Monkman-Grant function of time to failure for the various creep tests conducted to date.

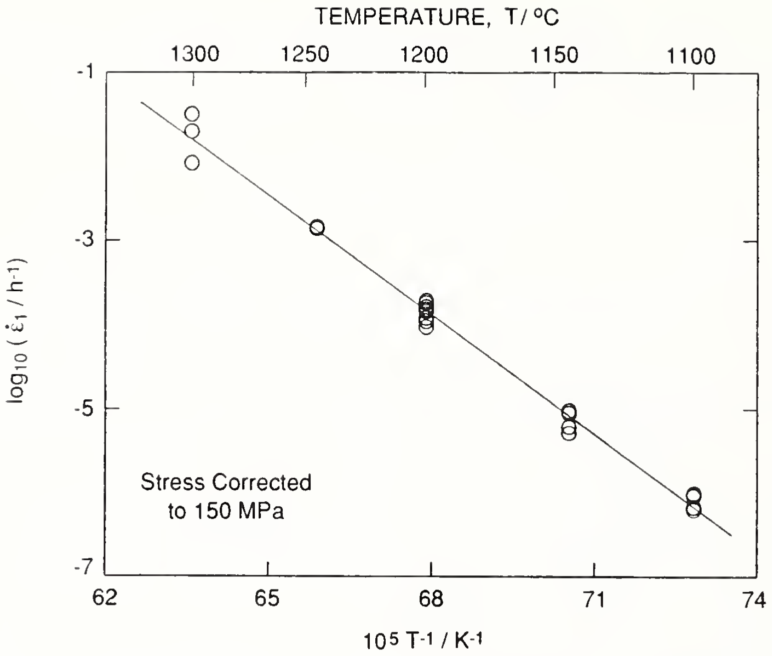

Figure 9. Secondary creep-strain rate as Arrhenius' function of temperature. The points which were observed at initial stresses other than 150 MPa were stress-corrected to 150 MPa. The solid line is a least-squares fit.

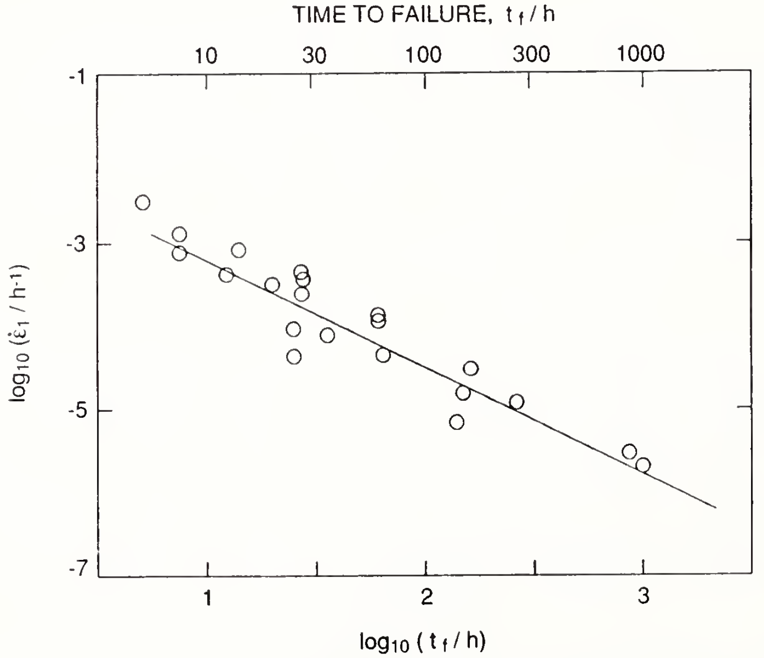

Figure 10. Secondary creep-strain rate as Monkman-Grant's function of time to failure. The solid line is a least-square fit.

B. Microstructure of Crept SiC_w/Al_2O_3 Composites

Summary. The creep data presented and analysed in the previous section displayed two different types of behavior. The strain rates of specimens tested at lower stresses decreased with time to extremely low values which did not follow the linear log strain rate/log stress relationship which was fitted to the high stress data. The low stress specimens failed after considerably longer times than the higher stress specimens for which the minimum strain rates were orders of magnitude higher. The microstructures of as-received specimens and specimens crept to failure have been studied using optical and electron microscopy to determine the mechanisms of creep and the reasons for the two regimes of behavior. Transmission electron microscopy has shown that both as-received material and creep-ruptured specimens contained cavitation at the whisker/Al_2O_3 grain boundary intersections to varying degrees. However, high stress specimens contained broken whiskers whereas those from the low stress regime did not. Based on these microstructural observations, the material has been modeled as an arrangement of elastic and viscous elements, and the predictions of this model are compared with the data analysis presented in the previous section.

Experimental Techniques and Results. Polished sections of the various specimens were prepared using standard metallographic techniques; the final polish was performed using 6 μm diamond paste. Specimens for transmission electron microscopy (TEM) were prepared from the as-received material and from the regions of the ruptured test specimens between the loading rollers. A diamond saw was used to cut thin slices parallel to the tensile surface. Disks 3 mm in diameter were ultrasonically cut from the slices and the disks were ground, dimpled, and ion-milled to perforation.

Polished sections of the as-received composite were studied in the optical microscope. Sections normal (Fig 11a) and parallel (Fig. 11b) to the hot-press axis revealed that the material was inhomogeneous and that the inhomogeneity was textured. Regions of the composite with a relatively high density of whiskers are separated by bands about 5 to 10 μm wide with a lower whisker fraction. The high whisker density regions are equiaxed in

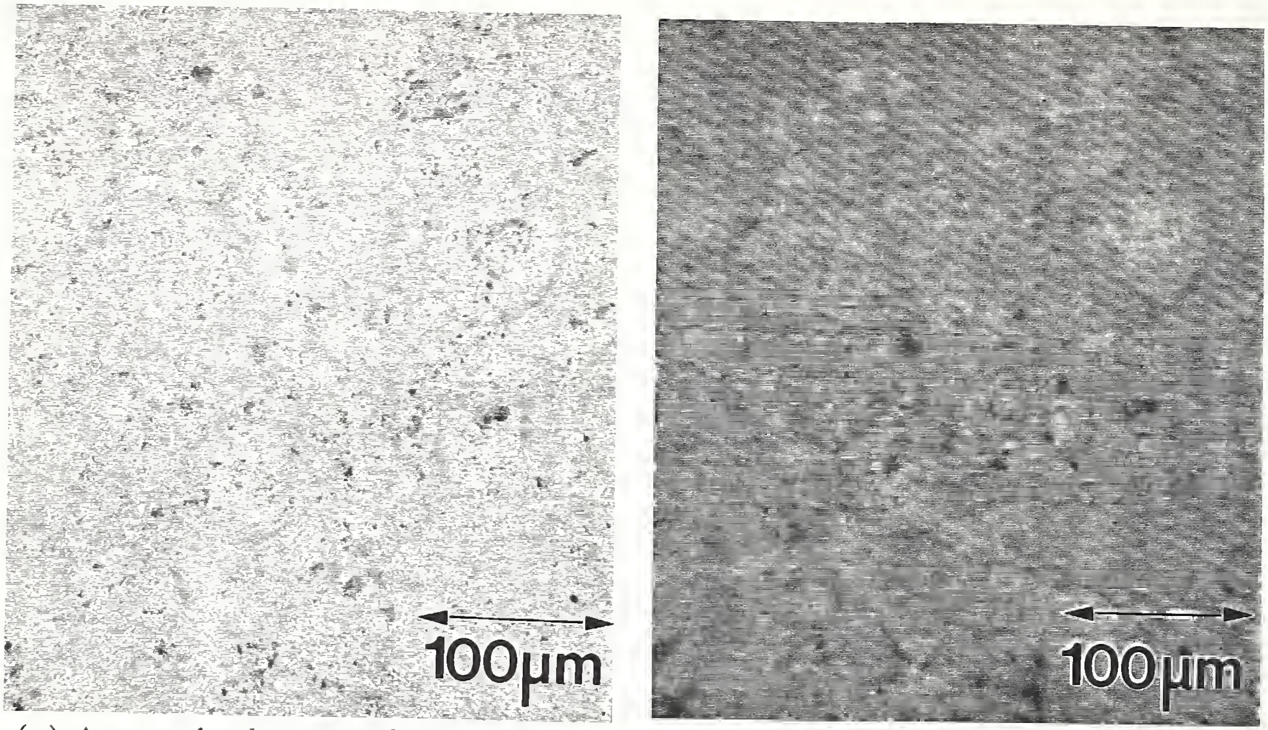

(a) As-received material normal to hot-press axis with reflected light.

(c) As-received material, same field as (a) with crossed polarizers.

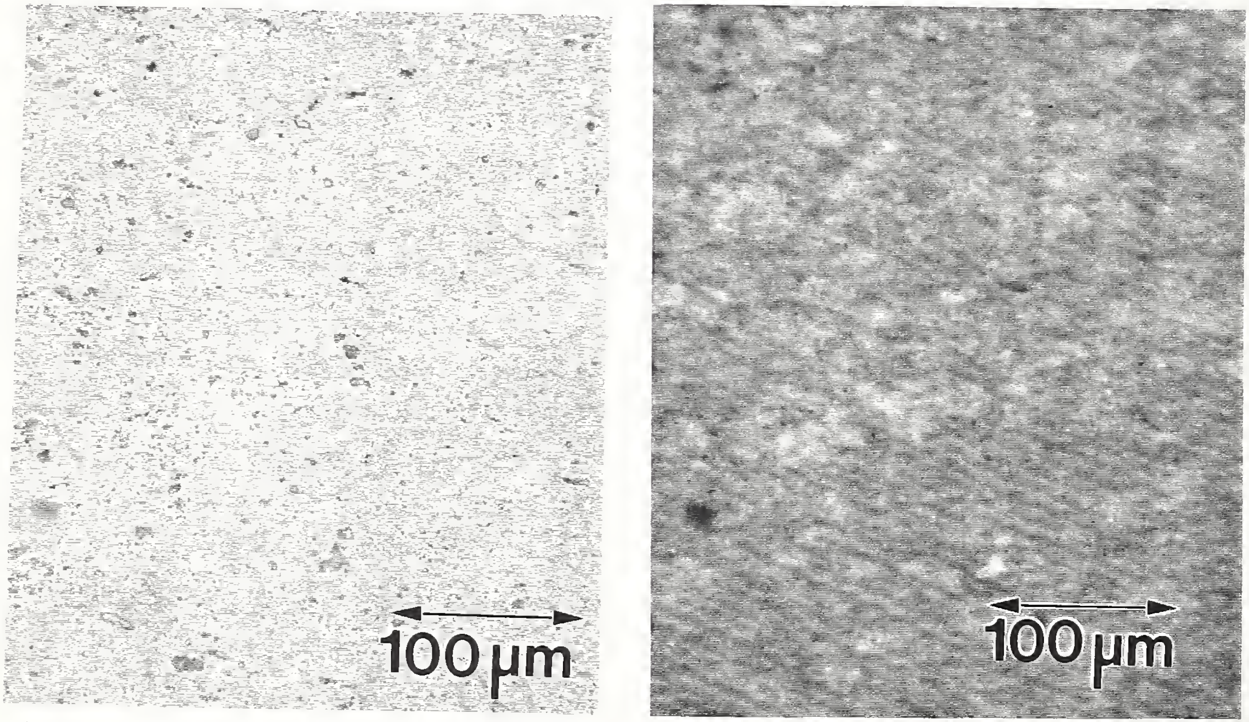

(b) As-received material parallel to hot-press axis with reflected light.

(d) As-received material, same field as (b) with crossed polarizers.

Figure 11. Optical micrographs.

the plane normal to the hot-press axis (Fig. 11a), but the section parallel to the hot-press axis (Fig. 11b) indicates that the high whisker density regions were compressed along the hot-press axis during processing. The material also contained voids 2 to 10 μm in diameter. Imaging the material under crossed polarizers highlighted the inhomogeneity in whisker density by causing the regions of high whisker density to appear lighter than the low density regions as can be seen in Figs. 11c and 11d which are of the same regions as Figs. 11a and 11b respectively.

Optical microscopy of specimens crept to failure at 1300°C with initial applied outer fibre stresses of 55 MPa, 100 MPa and 117 MPa was carried out on polished sections <u>normal</u> to the tensile/compressive axis. There was no evidence of cracking at the tensile surface in the crept specimens and no detectable difference in gross cavitation between the as-received and crept material. It has been pointed out that to observe evidence of damage in the optical microscope or the SEM (cracking and gross cavitation), it is more profitable to study sections <u>parallel</u> to the tensile/compressive axis and normal to the tensile surface[8]. This work is in progress.

TEM examination of the as-received material revealed intragranular pores in the Al_2O_3 and cavities at some of the triple junctions between whiskers and Al_2O_3 grain boundaries. However, most of the 4.9% porosity was accounted for by the large pores observed in the optical micrographs (Fig. 11). Pockets of glass were often observed at Al_2O_3 grain boundary/SiC whisker triple junctions and along the Al_2O_3/SiC interface as shown in the diffuse dark field micrograph in Fig. 12.

Fig. 13 is a low magnification TEM micrograph of a specimen crept at 1300°C and 72 MPa and is typical of all the specimens studied. The large variation in thickness is caused by the porosity and the inhomogeneous distribution of whiskers. It was observed that isolated SiC whiskers sputtered away more rapidly in the ion-miller than the surrounding Al_2O_3, but there was also evidence that regions of the specimen with low whisker density sputtered more rapidly. These two pieces of data appear to be contradictory, but may be explained by the residual stresses that result from the thermal contraction mismatch between SiC and Al_2O_3 which would be higher in the high whisker density regions. It is speculated that the

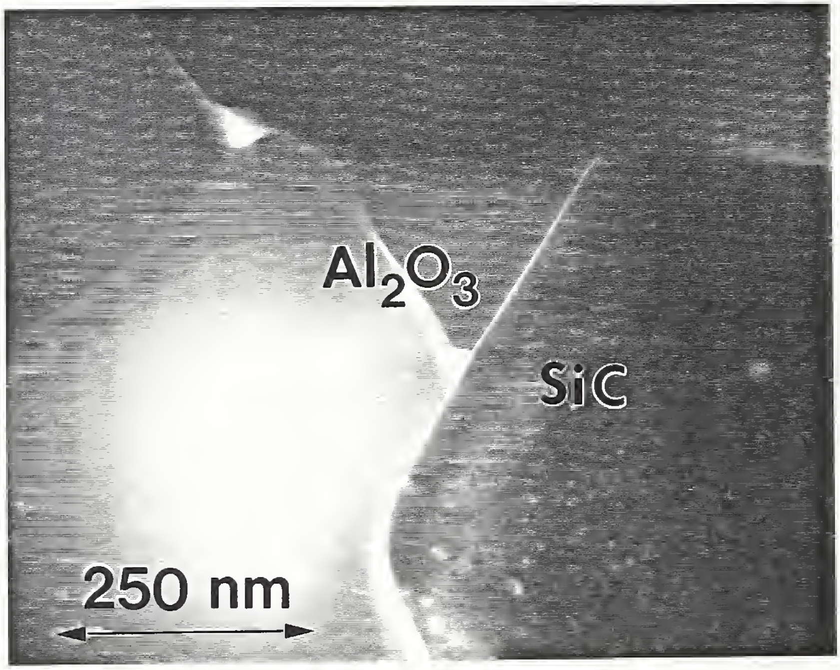

Figure 12. Diffuse dark field TEM micrograph of Al_2O_3 grain boundary/SiC whisker intersection with glassy phase at triple junction and along interface.

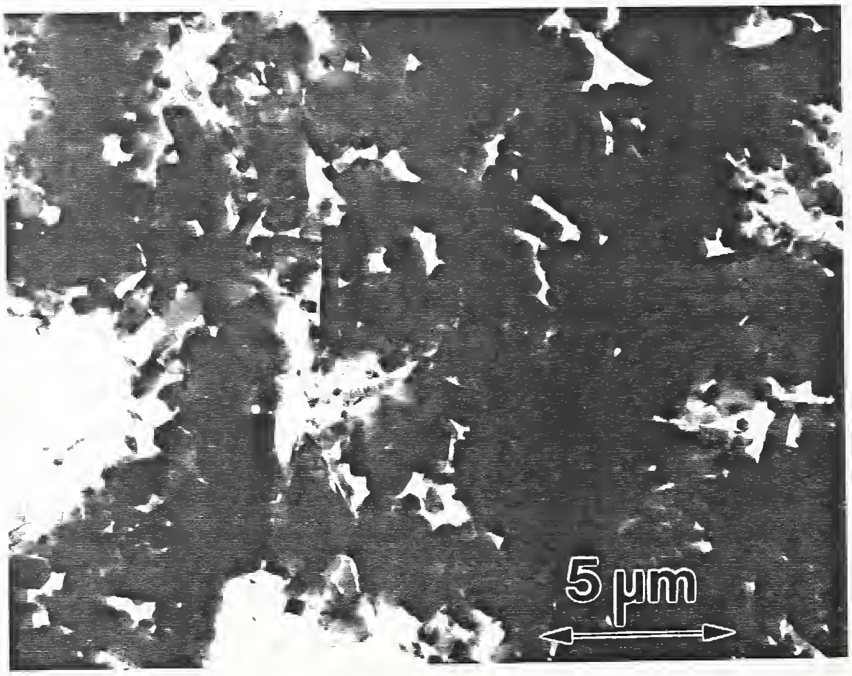

Figure 13. Low magnification TEM micrograph of specimen crept at 1300°C and 72 MPa showing much cavitation and significant variations in specimen thickness.

residual elastic stresses might lead to a lowering of the sputtering rate.

TEM observations were made on the microstructure of several specimens tested at 1300°C, specifically the 62 MPa (1), 72 MPa (2) and 98 MPa (3) specimens. These specimens had failure times/strains of 1001 h/1.07%, 28 h/1.85% and 5 h/1.98% respectively. Specimen (1) comes from the low stress regime and the other two from the high stress regime; the applied stresses differ by only 58%, but the failure times range over more than two orders of magnitude. Despite the large differences in time-to-failure for these three specimens, there was little difference between the level of cavitation observed at the Al_2O_3/SiC triple junctions, although qualitatively the level of cavitation appeared to be greater than in the as-received material. However, specimens (2) and (3) both contained broken whiskers, whereas specimen (1) did not. Figs. 14 and 15 from near the tensile and compressive surfaces of specimen (3) clearly show broken whiskers; the two fracture surfaces can be seen to have the same morphology. Cavitation and broken whiskers were the principal evidence of deformation observed in these specimens. Little dislocation activity was observed in the specimens beyond small angle grain boundaries in a few of the larger Al_2O_3 grains. However, since several specimens were tested in the same furnace at the same time, the specimens were not necessarily removed from the furnace immediately after failure; in some cases specimens were held at test temperature for several hours after failure, so it is possible that any dislocations generated during creep were annealed out of the Al_2O_3 grains before the dislocation structure was frozen in.

Discussion. Apart from whisker fracture, there was little difference in microstructure between the three ruptured specimens that could be observed by TEM. (It should be noted that TEM is never a truly quantitative method of characterizing microstructures). Despite the considerable differences in their failure times, the failure strains of the three specimens are within a factor of two of each other. It is suggested that sliding at Al_2O_3/SiC interfaces and cavitation caused by the incomplete accommodation of the sliding were the primary deformation mechanism in all the specimens. In specimen (1) where no whisker fracture occurred, the whisker network retained its original strength, and, once the

Figure 14. TEM micrograph taken from near tensile surface of specimen crept at 1300°C and 98 MPa showing whisker fracture.

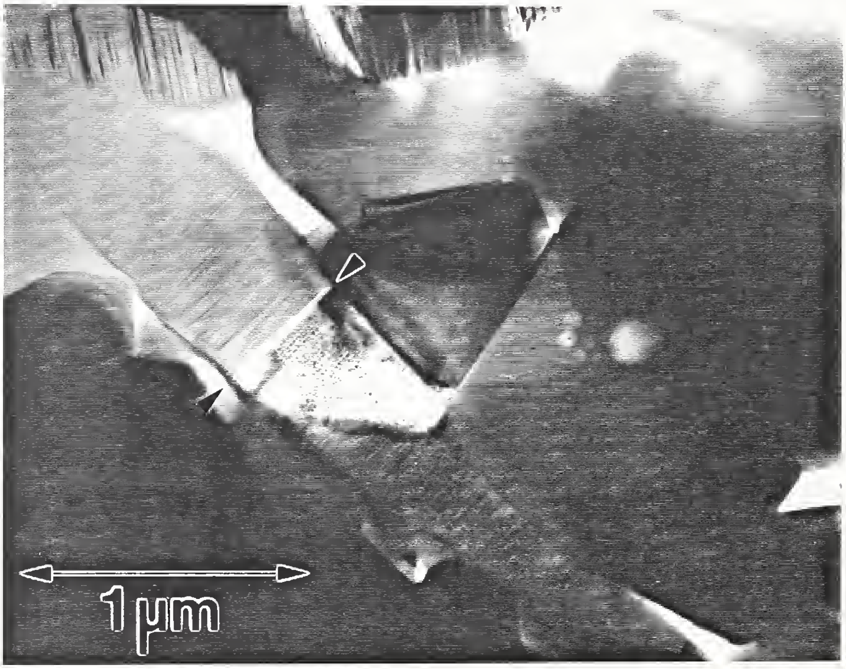

Figure 15. TEM micrograph taken from near compressive surface of specimen crept at 1300°C and 98 MPa showing whisker fracture.

stress had been transferred to the network by creep of the alumina, the deformation of the specimen practically ceased. In specimens (2) and (3) where the applied stresses were higher, fracture of whiskers resulted in a decreasing strength for the network and continuing creep deformation with time.

Porter[9] has suggested that these composite materials, in their response to an applied stress, can be modeled as an elastic element (the network of SiC fibers) in parallel with a viscous element (dashpot A) representing the alumina matrix, this Kelvin-Voigt compound element being in series with another viscous element (dashpot B) representing the non-recoverable deformation of the composite which is caused by broken whiskers. The stress response of the Kelvin-Voigt compound element consists of shedding load from dashpot A to the spring which eventually supports all the load such that the steady state strain rate is zero. Dashpot B deforms at a steady state. This model was used in the previous section to analyze the experimental data with some success. The agreement between experimental data and the model are best for short times and at high stresses.

The observations of the deformed specimens described above lead to the suggestion of a different model. This consists of a Kelvin-Voigt compound element with the addition of a highly non-linear dashpot (C) in series with the spring to model the effect of whisker fracture. The observations indicate that at low applied stresses the whiskers in the composite do not break. Therefore dashpot C does not deform and the model reduces to a Kelvin-Voigt element for which the steady state strain rate is zero. When the applied stress is high enough to cause whisker fracture, the effective elastic modulus of the whisker network begins to decrease in a way which is non-linear in both time and stress and can be modeled by the flow of a non-linear dashpot.

Chuang et al.[10] have analysed the flexural creep of a bend test bar which they model as an array of identical compound elements aligned with the bar and arranged across the bar from the tensile to compressive surfaces. They considered the case of a Maxwell element, i.e. a spring and dashpot in series, and allowed for the fact that creep in tension and compression typically have different stress exponents. The equilibration of stress among the elements in such a model is a complex time-dependent process with a time constant that varies as σ_a^{1-n} where σ_a is the initial applied stress and n is the compressive stress creep exponent. Thus the time to establish steady state flexural creep rises as the initial applied stress falls although the exact dependence on stress cannot be given, as accurate data for n are not available. For all stresses, the time taken to establish steady state flexural creep is at least an order of magnitude larger than for tensile or compressive creep. The extension of this technique to different models, in particular the modified Kelvin-Voigt element described above, is under consideration.

Conclusions. The creep data for SiC whisker-reinforced Al_2O_3 presented in the previous section show two different regimes of response to a range of applied stresses at a given temperature. The creep strain versus time data have been fitted to a rheological equation that is based on a reasonable viscoelastic model of the composite material. The secondary creep-strain rate data in the high-stress regime have been analyzed, using Norton's power-law function of stress and Arrhenius' inverse-temperature function. Transmission electron microscopy of ruptured specimens in the two regimes indicates that specimens tested at higher stresses contain broken whiskers whereas lower stress specimens do not. It is suggested that below a threshold stress for whisker fracture the material tends to a steady state strain rate of zero, but above this stress whisker fracture leads to continuing deformation culminating in rupture. Based on the microstructural observations, a modified Kelvin-Voigt model for the creep behavior of the composite has been proposed.

REFERENCES

1. E.R. Fuller, Jr., R.F. Krause, Jr., M.D. Vaudin, and T.R. Palamides, "Toughening Mechanisms in Ceramic Composites," NISTIR 88-4018, National Institute of Standards and Technology, Gaithersburg, MD, February 1989; also in ORNL/FMP-88/2, Fossil Energy Materials Program, R. R. Judkins, Manager, Oak Ridge National Laboratory, Oak Ridge, TN, 1989, pp. 115-134.

2. T.W. Coyle, E.R. Fuller, Jr., P. Swanson, and T.R. Palamides, "Fracture Mechanics Characterization of Crack/Fiber Interactions in Ceramic Matrix Composites," Ceram. Eng. Sci. Proc. 8 [7-8] 630-635 (1987).

3. T.W. Coyle, T.R. Palamides, S.W. Freiman, E.R. Fuller, Jr. and U.V. Deshmukh, "Crack-Fiber Interactions in Ceramic Matrix Composites," in Proceedings of Conference on High Temperature Structural Composites: Synthesis, Characterization and Properties, The Metallurgical Society, 1987 Northeast Regional Meeting, Hoboken, N.J. May 27-29, 1987.

4. F.H. Norton, "The Flow of Ceramic Bodies at Elevated Temperatures," J. Amer. Ceram. Soc. 19 129-134 (1934).

5. G.W. Hollenberg, G.R. Terwilliger, and R.S. Gordon, "Calculation of Stresses and Strains in Four-Point Bending Creep Tests," J. Amer. Ceram. Soc. 54 196-199 (1971).

6. P.G. McVetty, "Working Stresses for High Temperature Service," Mech. Eng., A.S.M.E, 56 149-154 (1934).

7. F.C. Monkman and N.J. Grant, "An Empirical Relationship between Rupture Life and Minimum Creep Rate in Creep-Rupture Tests," Proc. Amer. Soc. Test. Mater. 56 593-620 (1956).

8. P. Angeline, private communication, 1989.

9. J.R. Porter, "Observations of Non-Steady State Creep in SiC Whisker Reinforced Alumina," in Proceedings of Conference on Whisker- and Fiber-Toughened Ceramics, ASM International and Oak Ridge National Laboratory, Oak Ridge, Tennessee, June 7-9, 1988.

10. T.-J. Chuang, S.M. Wiederhorn and C.F. Chen, "Transient Behavior of Structural Ceramics Under Flexural Creep," in Creep and Fracture of Engineering Materials and Structures, edited by B. Wilshire and R.W. Evans, Proceedings of the Third International Conference held at University College, Swansea, April 5-10, 1987, The Institute of Metals, London.

NIST-114A
(REV. 3-89)

U.S. DEPARTMENT OF COMMERCE
NATIONAL INSTITUTE OF STANDARDS AND TECHNOLOGY

BIBLIOGRAPHIC DATA SHEET

1. **PUBLICATION OR REPORT NUMBER**
NISTIR-89-4111

2. **PERFORMING ORGANIZATION REPORT NUMBER**

3. **PUBLICATION DATE**
August 1989

4. **TITLE AND SUBTITLE**
Toughening Mechanisms in Ceramic Composites
Semi-Annual Progress Report for the Period Ending March 31, 1989

5. **AUTHOR(S)**
E. R. Fuller, Jr., E. P. Butler, R. F. Krause, Jr., and M. D. Vaudin

6. **PERFORMING ORGANIZATION (IF JOINT OR OTHER THAN NIST, SEE INSTRUCTIONS)**
U.S. DEPARTMENT OF COMMERCE
NATIONAL INSTITUTE OF STANDARDS AND TECHNOLOGY
GAITHERSBURG, MD 20899

7. **CONTRACT/GRANT NUMBER**
DE-AI05-800R20679

8. **TYPE OF REPORT AND PERIOD COVERED**
Interim

9. **SPONSORING ORGANIZATION NAME AND COMPLETE ADDRESS (STREET, CITY, STATE, ZIP)**
U. S. Department of Energy, Fossil Energy, Advanced Research & Technology Development, Fossil Energy Materials Program, Oak Ridge National Laboratory, Oak Ridge, TN

10. **SUPPLEMENTARY NOTES**

☐ DOCUMENT DESCRIBES A COMPUTER PROGRAM; SF-185, FIPS SOFTWARE SUMMARY, IS ATTACHED.

11. **ABSTRACT (A 200-WORD OR LESS FACTUAL SUMMARY OF MOST SIGNIFICANT INFORMATION. IF DOCUMENT INCLUDES A SIGNIFICANT BIBLIOGRAPHY OR LITERATURE SURVEY, MENTION IT HERE.)**

A silicon carbide fiber used as reinforcement in a borosilicate glass matrix has been shown to enhance the fracture toughness of the glass by as much as 22%. A ductile nickel coating on the fiber was found to reduce the interfacial shear strength and the frictional sliding between the fibers and the glass matrix, but any influence that the thickness of the nickel coating has on toughening was not conclusive.

Time functions of creep strain and creep times to failure were measured for a 25 wt% SiC whisker-reinforced Al_2O_3 composite with 4.9% porosity. Beam specimens were used in four-point flexure with variously fixed bending moments and fixed temperatures between 1100 and 1300°C. The results were analyzed to evaluate secondary creep-strain rate as a function of stress on the outer fiber, of temperature, and of time to failure.

The secondary creep-strain rates of specimens tested at lower stresses did not follow a power-law function of stress which was fitted to the high stress data. The microstructure of as-received specimens and specimens crept to failure were studied using optical and electron microscopy to determine the mechanisms of creep in the two stress regimes. Both kind of specimens contained cavitation at the whisker/Al_2O_3 grain boundary intersections to varying degrees. However, high stress specimens contained broken whiskers whereas those from the low stress regime did not.

12. **KEY WORDS (6 TO 12 ENTRIES; ALPHABETICAL ORDER; CAPITALIZE ONLY PROPER NAMES; AND SEPARATE KEY WORDS BY SEMICOLONS)**

bridging; ceramic; composites; crack; creep; creep rupture; fibers; fracture toughness; interfaces; toughening; whiskers

13. **AVAILABILITY**
XX UNLIMITED
☐ FOR OFFICIAL DISTRIBUTION. DO NOT RELEASE TO NATIONAL TECHNICAL INFORMATION SERVICE (NTIS).
☐ ORDER FROM SUPERINTENDENT OF DOCUMENTS, U.S. GOVERNMENT PRINTING OFFICE, WASHINGTON, DC 20402.
☐ ORDER FROM NATIONAL TECHNICAL INFORMATION SERVICE (NTIS), SPRINGFIELD, VA 22161.

14. **NUMBER OF PRINTED PAGES**
28

15. **PRICE**
$12.95

ELECTRONIC FORM